The final publication is available at

https://doi.org/10.1016/j.compstruct.2021.114360

Additional Information

On the effect of geometrical fiber arrangement on damage initiation in CFRPs under transverse tension and compression

Miguel Marco[a], Eugenio Giner[b], María Henar Miguélez[a], David González[c]

[a] *Department of Mechanical Engineering, Universidad Carlos III de Madrid, Avda. de la Universidad 30, 28911 Leganés, Madrid, Spain*
[b] *CIIM-Department of Mechanical and Materials Engineering, Universitat Politècnica de València, Camino de Vera, 46022 Valencia, Spain*
AFRC-National Manufacturing Institute Scotland, University of Strathclyde, 85 Inchinnan Drive, Renfrewshire, PA4 9LJ, UK
*Corresponding author. E-mail: xxxx@xxxxx.com

Abstract

The mechanical performance of composite materials is strongly dependent on its microstructure. Efficient design of composites requires proper estimation of the effect of the microstructure on residual stresses that arising from cooling due to manufacturing temperature. The study of the stresses and damage in fibres interface and its relationship with geometrical distribution of the fibres can contribute to a better comprehension of the mechanical response of the composite.

We use 2D numerical models to represent a composite material reinforced with longitudinal fibres. The mechanical behaviour is analysed taking into account the cooling effect and tension/compression transverse loading. We have generated a range of virtual microstructures, characterized by the microstructure randomness, to study the influence of the fiber randomness on the damage initiation. Damage initiation at fibres interfaces has been estimated from the stresses induced at the interface, both in the whole structure and for individual fibers.

As expected, a strong effect of the randomness of the fiber arrangement on the damage initiation has been found. For all microstructures and loading modes, higher values of microstructure randomness results in earlier damage development. Normal and shear stresses at individual fibre interfaces have been analysed under tension and compression loading. In tension, normal stress at the fiber interface fully dominates the interfacial damage initiation. In compression, damage is almost completely dominated by the interfacial tangential stress. In compression, localized plasticity develops simultaneously with damage initiation whereas

in tension, damage initiation occurs at a stress three times lower than the required for the onset of plasticity. The maximum shear and normal stresses around individual fibers are strongly affected by the local neighborhood.

Keywords: Interface damage, random fiber distributions, cooling effect, periodic boundary conditions

1. Introduction

The compressive strength properties in unidirectional carbon fibre-epoxy laminates are often less than 60% of their tensile strengths, when the loading axis is aligned with the fiber axis [2]. The compressive strength is severely affected by the transverse behaviour where microbuckling of the fibers can lead to damage nucleation. This transverse fracture involves a crack growing perpendicular to the loading direction, for a sample loaded in the same direction as the direction of the fibres (see Fig. 1.1). Transverse fracture is often the first failure mechanism that occurs early in the loading stage of composite structures [15].

Carbon fiber reinforced polymers (CFRPs) have been studied under longitudinal compression combined with shear conditions in the transverse plane [7, 32]. It was observed that in all combinations of shear and compression considered, microbuckling of the fibers resulted in localized plastic deformation in the matrix forming narrow bands. In the case of tensile stresses perpendicular to the fibers, cracks appear orthogonal to the tensile axis [3]. In the case of compression perpendicular to the fibers, final failure is due to localized plastic deformation in the matrix [10]. In [13], damage has been observed in metal-matrix laminates under shear loading on the transverse plane to the fibers. Hinz et al. [13] concluded that local high stress concentrations due to the fibre arrangement and small inter-fibre distances are the cause of localized interfacial damage.

The cooling down effect from manufacturing temperature induces residual stresses (RS) (due to the material thermal anisotropy of fiber-matrix composite) that superimpose on the applied stress during service. As in the case of tensile stresses perpendicular to the fibers [3], the interfacial failure leads to the formation of a crack perpendicular to the fiber axis. The microstructure can have a great effect on damage initiation in terms of the location of the damage within the microstructure [31]. Fig. 1.1 shows examples of interfaces damage

2

at first stages of debonding due to geometrical arrangement [13] and final interfacial crack propagation [27].
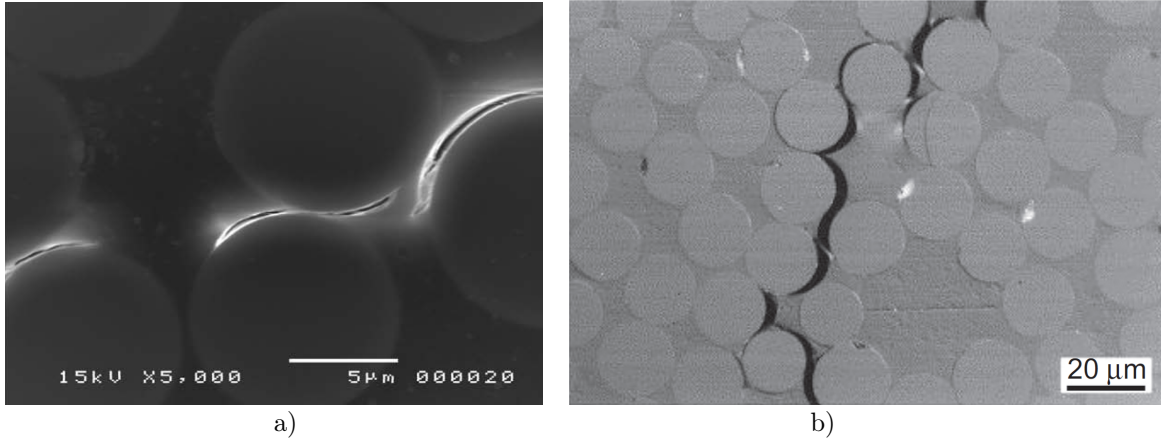

Figure 1.1: Interface damage in longitudinal fibres composites. a)Fibre/matrix debonding due to local fibre configuration [13]. b) Crack formation through damaged interfaces [27]. Reprinted from Refs. [13, 27] with permissions.

Tomography are increasingly used for non-destructive 3D damage observation in composites [8]. This technique can also reveal fibre-matrix interfacial damage and interlaminar damage in cross-ply laminates [26]. However, local plasticity and micro voids that may occur at the matrix-fibre interface are difficult to notice experimentally. For example, the poor contrast between fibres and matrix limits the localization of narrow matrix cracks, even at high spatial resolution [8]. In order to optimize the composite microstructure, testing campaigns can be accompanied of non-destructive testing to explore damage development. However this repetitive testing strategy is costly and time consuming. Moreover, extracting conclusions from experimental results can be challenging unless careful repeatability is maintained in terms of material microstructure, manufacturing route and testing conditions [18]. Thus, a systematic and accurate method is needed to estimate the effect of microstructure on damage development during loading. In recent years, virtual testing has shown potential as an alternative strategy to costly repetitive testing and mechanical behaviour estimation [17, 9].

Numerical studies have demonstrated the strong effect of the interface on the general strength of the composite materials [31]. Fibre-matrix interface defects [4] and micro-voids [29] can also affect the damage initiation in CFRPs. Additionally, the transverse in-plane shear behaviour has been shown to be greatly

affected by the fibrematrix interface strength [28]. However, fewer studies have focused on the effect of other intra-ply properties such as the local fibre distribution [14, 9], or the thermal expansion mismatches leading to residual stress. Numerical studies have investigated the effect of particle clustering on the mechanical behaviour in metal-matrix composites with spherical reinforcements [24, 25]. Previous analyses have shown that the randomness of the positioning of the fibers has little impact on the macroscopic stress-strain responses for uniaxial stress and shear testing [28]. However, the arrangement of fibers when manufacturing CFRPs can play a significant role on fiber debonding upon transverse mechanical loading [13, 31] and transverse mechanical behaviour [9]. In this regard, the relationship between the geometrical arrangement fibers and the interfacial normal stresses under transverse loading has been investigated for CFRPs [14]. It was found that, for an irregular fibre array, the absolute value of the interfacial normal stresses rapidly increased when the distance between fibres was less than 0.5μm [14]. However, the in-plane shear contribution to damage was not considered nor the evolution of damage initiation as a function of the macroscopic load. In order to find appropriate relationships between microstructure and mechanical properties, the effect of geometrical arrangement of fibers on the damage initiation at the interfaces should be understood.

In this paper, systematic study of the effect of fiber arrangement on the damage caused by the combination of normal and shear stresses at the interface is presented. The loading is applied after a previous simulation step where residual stresses arising from cooling are induced; manufacturing temperature is considered in this work. This methodology is employed for the "virtual testing" of a variety of composite microstructures in terms of the randomness of the fiber arrangement. To the best of our knowledge, this is the first time that the effect of randomness on damage initiation and residual stresses due to the cooling are systematically studied in CFRPs using Representative Volume Elements (RVEs).

2. Numerical model

2.1. Material properties and interface damage initiation criteria

The material properties assigned in this work correspond to the AS4/Epoxy 8552 CFRP composite unidirectional laminate. This composite is widely used and most of its properties can be found in the

literature. The elastic and plastic properties of the matrix, fibers and interface can be found through nanoindentation techniques and micromecanical testing [21, 22, 19]. The material properties used for this work are shown in Tables 1 and 2. The fibers are assumed to behave as elastic orthotropic solids with elastic behaviour (note that 11 is the longitudinal axis of the fibers, while 23 is the transverse plane to them). The matrix is modelled as an elasto-plastic rate-independent solid without hardening or softening. The Drucker−Prager model [5], originally developed for soils, defines a pressure dependent yield surface which is smoother than the Mohr-Coulomb yield surface. This implies that the yield in uniaxial tension, σ_{yt}, may be different to the yield under uniaxial compression, σ_{yc}. The yield surface is defined as:

$$f_{DP}(\sigma, \beta, \sigma_0) = \sigma_e - \sqrt{3}\sigma_0 + \beta\sigma_m \tag{2.1}$$

where σ is the stress tensor and σ_e, σ_m the effective and mean stresses respectively. σ_0 and β are material constants. By substituting (2.1) with the values of σ_e, σ_m for the stress state corresponding to of σ_{yt} and σ_{yc} it is found:

$$\sigma_0 = \frac{2}{\sqrt{3}}\left(\frac{\sigma_{yc}\sigma_{yt}}{\sigma_{yc} + \sigma_{yt}}\right) \quad \text{and} \quad \beta = \sqrt{3}\left(\frac{\sigma_{yt} - \sigma_{yc}}{\sigma_{yc} + \sigma_{yt}}\right) \tag{2.2}$$

The yield function is found by substituting σ_{yc} and σ_{yt} from Table 1 into equations (2.2) and (2.1). Note that if $\sigma_{yt} = \sigma_{yc}$ then $\sigma_0 = \sigma_{yt}/\sqrt{3}$ and $\beta = 0$, recovering von Mises plasticity upon substitution of σ_0 and β on equation (2.1). Mechanical properties of the matrix are shown in Table 1, including normal and shear strength, σ_n and τ, respectively.

E[GPa]	ν	σ_{yt}[MPa]	σ_{yc}[MPa]	α [K^{-1}]	σ_n[MPa]	τ[MPa]
5.07	0.35	121	176	$5.2e-5$	42	63

Table 1: Parameters defining the material behaviour for the 8552 Epoxy matrix and damage interface properties σ_n and τ.

Cohesive zone models have the proved the ability for addressing a variety of crack analyses since they were introduced in the 1960s [6]. However, when these elements are inserted between two media (matrix and interface) with different elastic properties having a finite thickness, the chosen interfacial properties may

5

E_1 [GPa]	$E_2 = E_3$ [GPa]	ν_{12}	ν_{13}	$G_{12} = G_{13}$ [GPa]	G_{23} [GPa]	α_1 [K^{-1}]	$\alpha_2 = \alpha_3$ [K^{-1}]
231.6	12.97	0.3	0.46	11.3	4.45	$-9 \cdot 10^{-7}$	$7.2 \cdot 10^{-6}$

Table 2: Elastic stiffness constants and thermal expansion properties for the AS4 fibers.

affect the load transfer (matrix to fibers in CFRPs) [20, 16, 31]. This effect of the interface properties is magnified when several concurrent cohesive elements share nodes in 3D [11]. For these reasons, and noting that this work is only focusing on the early stages of damage initiation, we have opted to read the stress values at the Gauss points of the contiguous elements to the interface placed in the matrix, without introducing cohesive elements and therefore without damage modelling. Stresses are analysed in the matrix, since it is the weakest material in the composite. From the interfacial stress values we use a classical failure model for composites used by Hashin [12, 1] to estimate interfacial damage, defined as:

$$\left(\frac{\langle t_{\mathrm{n}} \rangle}{\sigma_{\mathrm{n}}}\right)^2 + \left(\frac{t_{\mathrm{s}}}{\tau}\right)^2 = 1 \tag{2.3}$$

where $\mathbf{t}$ is the vector normal to the interface and t_{n} and t_{s} are normal and tangential stress components of $\mathbf{t}$ respectively. The interfacial strengths, σ_{n} and τ were defined in Table 1. The Macaulay brackets $\langle \rangle$ are defined as $\langle t_{\mathrm{n}} \rangle = \frac{1}{2}\left(t_{\mathrm{n}} + |t_{\mathrm{n}}|\right)$, ensuring t_{n} only contributes to damage in tension. The values used for interfacial strength are similar to those observed experimentally in [13, 31].

2.2. Finite element mesh and boundary conditions

Each microstructure studied consists of a 2-dimensional RVE containing 30 fibers. For consistency, we maintain the same number of fibers and the same volume fraction $V_{\mathrm{f}} = 0.5$ for all microstructures. Final dimensions of the model are:

$$\begin{aligned} \text{width; } w = 5d_w = 5\sqrt{\frac{2\pi}{\sqrt{3}}}\frac{r}{\sqrt{0.5}} \\ \text{high; } h = 6d_h = 6\sqrt{3}\frac{d_w}{2} \end{aligned} \tag{2.4}$$

where d_w and d_h are geometrical dimensions of hexagonal distribution and r is the fiber radius. The model has been built using also a periodic microstructure, implying that a repetition of the unit cell to adjacent edges to the RVE (4 edges in 2D) maintains the macroscopic properties. The model is built as a plane strain problem since we represent a thick specimen with cylindrical fibers aligned normal to the plane of analysis. The RVE including fibers and matrix consists of about 27,000 Abaqus CPE3 single Gauss point elements. Size element is one that leads to about 8 elements in the fiber radius. A detail of a fiber meshed is shown in Fig. 2.1. In this figure we also explain what we call segments, element lateral sides in the interface where we calculate the stresses and where we quantify the damage in the interface. The angle θ will be used in next sections to analyse its influence on the stresses along the interface.
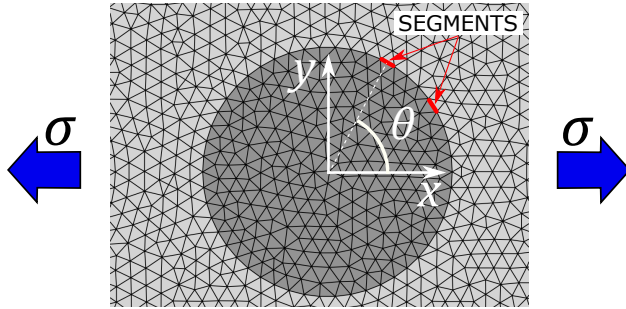

Figure 2.1: Mesh used on the model, segment and angle θ definition.

In order to ensure a model set-up with appropriate loading conditions, we have imposed periodic boundary conditions (PBCs) on the edges of the RVE. Two concurrent edges of the RVE with dimensions $L \times L$ are coincident with the coordinate axes X_1 and X_2. Then nodal displacement conditions between opposite faces of the RVE are imposed as follows:

$$\mathbf{u}(L, u_2) - \mathbf{u}(0, u_2) = \mathbf{u}_1^*$$

$$\mathbf{u}(u_1, L) - \mathbf{u}(u_1, 0) = \mathbf{u}_2^*$$

(2.5)

where $\mathbf{u}_1^*$ and $\mathbf{u}_2^*$ are the displacement of the master nodes. The nodal positions in the RVE satisfy $0 \leq u_i^* \leq L$ with $i = 1, 2$. Then, uniaxial tension can be applied by imposing appropriate displacements to the master nodes. To apply uniaxial tension in the X_1 direction via a stretch δ_1, the master nodes will have displacements: $\mathbf{u}_1^* = (\delta_1, 0)$, $\mathbf{u}_2^* = (0, p)$. The displacement p represent the macroscopic Poisson contraction of the RVE to

7

ensure equilibrium as follows:

$$\int_{\Omega} \mathbf{t}_2 \, d\Omega = 0 \ \text{ on } \ u_2 = L \tag{2.6}$$

where $\mathbf{t}_2$ is the normal traction acting on the edge $u_2 = L$.

The simulation involves cooling from the curing temperature (180ºC) to the service temperature (20ºC) for AS4/8552 CFRP. This is achieved by applying a change of temperature uniformly in the whole component, $\Delta T = -160$ºC. Upon cooling, a thermal residual stress appears owing to the mismatch of the thermal expansion constants of matrix and fibers. Following cooling, a uniaxial load is applied to the master node at $\mathbf{u}_1$ to reproduce transversal stress.

3. Randomness arrangement indicator (RAI) for fibers

An algorithm based on the distances between nearest neighbours fibers has previously been proposed to define the spatial randomness in virtual and existing microstructures [30]. In the present study, we propose the design of microstructures according to the level of randomness with respect to the hexagonal arrangement (honeycomb pattern). In order to keep consistently, we propose a single number that can characterize the level of randomness in each microstructure, based on the minimum distance between center of neighbouring fibers. This is achieved from the basis of a honeycomb arrangement and randomly oscillating each fiber in a random direction by a random amount in the interval $\delta d = 10^{-3} L$, where L is the characteristic size of the RVE. In Eq. 3.1 we define the RAI as the ratio between the distance from any fiber to the nearest neighbour and the distance between nearest fibers in a honeycomb arrangement. Although several methods can be used to develop a fiber random distribution, with this methodology we are able to control the randomness of the model from an hexagonal distribution with $RAI = 0.0$. In addition, we avoid overlapping between fibers due to the randomly distribution.

$$RAI = \frac{d_0 - d_{\min}}{d_0 - D} \tag{3.1}$$

8

Where d_0 is the initial distance between adjacent fibers in a honeycomb arrangement, $d_{\min}$ is the minimum distance between fibers in the randomly distribution and D is the fiber diameter. Thus, a microstructure with $RAI = 0$ means a perfect honeycomb arrangement, while $RAI = 1$ means the most random arrangement with contact between fibers and intermediate values for RAI mean an intermediate randomness. Some distributions with different $RAIs$ are shown in Fig. 3.1. Note that considering PBCs when a fiber exceeds one of the limits of the RVE it is included in the opposite side.
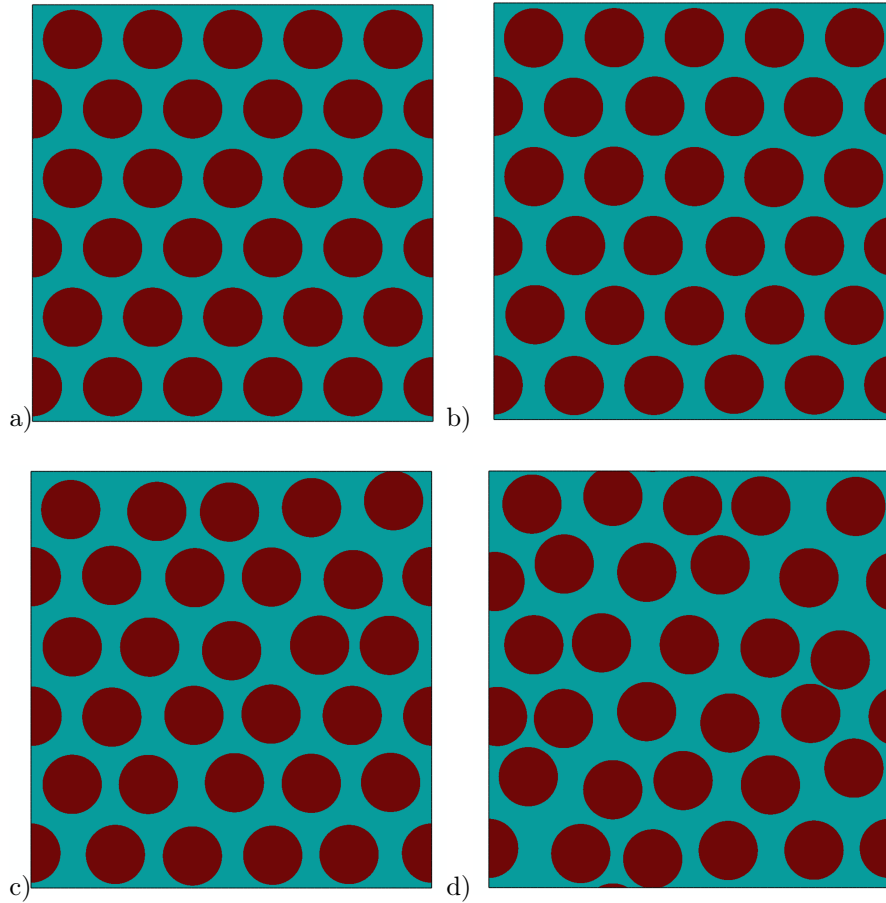

Figure 3.1: Random distributions developed for different values of the RAI parameter. a) $RAI = 0.0$, b) $RAI = 0.10$, c) $RAI = 0.5$, d) $RAI = 0.90$.

4. Results and discussions

4.1. Mesh density sensitivity

We analysed the mesh size influence in order to investigate an optimum relationship between computational cost and accuracy of results for the proposed microstructures. We further investigated the results using linear interpolation elements (CPE3 in Abaqus) and quadratic interpolation elements (CPE6 in Abaqus). We obtained similar results for both meshes when the mesh refinement for the linear interpolation elements was increased by a factor of 4 with respect to the number of quadratic interpolation elements, since both elements have similar computational behaviour. After these analyses we concluded that an element size of about $l = D/16$ is accurate enough for this work.

4.2. Residual stress analysis

Owing to the different expansion coefficients of fiber and matrix, residual stresses are induced on the interface between carbon fiber and matrix, which influence the microcrack nucleation [23]. For all microstructures, we observe an approximate hydrostatic pressure (not shown) of ≈ 30MPa in tension for matrix and compression for fibers despite the differences in fibre arrangement. However, for microstructures with high RAI number, there are local variations of stresses that can vary up to $\approx \pm 10$MPa in the vicinity of nearby interfaces (see Fig. 4.1). As for the RVE averaged thermal contraction, for the honeycomb type, the horizontal and vertical contractions are similar despite the directional asymmetry in the fibre arrangement.

The thermal residual stress map in the horizontal direction (without loading) is shown in Fig. 4.1 a for $RAI = 0.9$. The results show that the average stress in the horizontal direction in the fibers is around |25MPa| in tension and compression for matrix respectively (Fig. 4.1a). For microstructures with high RAI parameter, like the one shown in 4.1, there are local variations of $\approx \pm 15$MPa in the vicinity of nearby interfaces. This implies that interfaces can be left with significant compressive residual thermal stresses upon cooling (see compression areas in Fig. 4.1a), which would retard failure. Upon loading in tension (Fig. 4.1b, tension of 40.5 MPa), the fibers develop tensile stresses of ≈ 30MPa while the matrix increase the tensile stress to ≈ 60MPa, both with local variations of $\approx \pm 10$MPa. Instead, if loading in compression is applied

subsequent to cooling (Fig. 4.1d, compression of 109 MPa), the resulting stress field found varies across the RVE between slightly tensile ($\approx$ 5MPa) to highly compressive ($\approx$ 190MPa). The compression is generally accumulated in nearby horizontally-alligned fibers where the horizontal load is easily transmitted across the matrix. Low tensile stress is generally observed in the matrix below and above the fibers because the majority of the compression is being absorbed by the nearby highly-compressive bands running horizontally across matrix and fibers (Fig. 4.1d). These results are consistent with previous findings that indicate that thermal stresses can influence the initial location of damage in the microstructure upon loading [31]. We found that, for the selected loads, there was non existent plasticity under tension whereas localized plasticity appears when loading in compression. In the case of compression loading, the highly localized compression between nearby fibers leads to plasticity in the matrix (Fig. 4.1c).
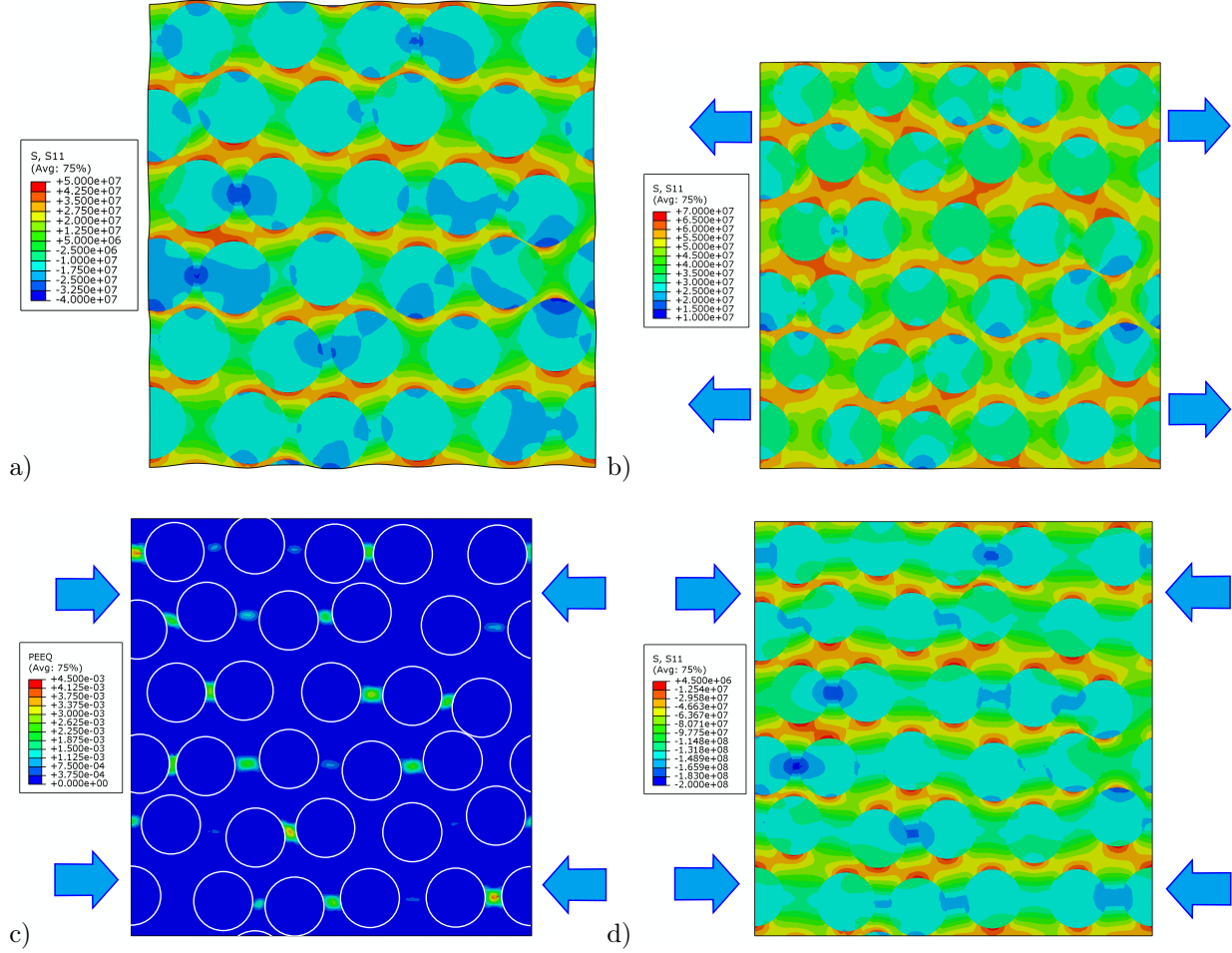
Figure 4.1: Contour plots with $RAI = 0.9$: a) stress field in the loading direction after cooling (stress expressed in Pa); b) stress field in the loading direction after subsequent loading (stress expressed in Pa; applied stress equal to 40.5 MPa); c) plastic equivalent strain contour plot in compression test at critical load (applied stress equal to 109 MPa, fibers marked with white lines) and d) stress field along the loading direction in compression test at critical load (stress in Pa; applied stress equal to 109 MPa).

4.3. Effect of fiber arrangement randomness on damage initiation

In this section we aim to show the evolution of the interfacial damage as a function of the applied load for each microstructure. As the tensile load is increased, the accumulated damage evolves according to the fraction of damaged segments at the interface. An interfacial segment is considered damaged when Eq. (2.3) is satisfied. Although the damage criterion in Eq. (2.3) is continuous, Fig. 4.2 shows a sharp increase in accumulated damage for all microstructures at ≈38-43 MPa for tension and at ≈95-120 MPa for compression.

Because we are only estimating the damage initiation and not the propagation, it is essential that the % of damaged segments remains small throughout our analyses to ensure the stress field is not significantly redistributed. Thus, we have only studied $RAIs \leq 0.9$ and loads that result in less than 2% of damaged segments. Following this damage initiation criteria, we find that damage has fully initiated for the $RAI = 0.9$ (percentage of damaged segments $\approx 2\%$) at 40.5 MPa in tension and 109 MPa in compression. Henceforth, these loads will be considered as reference values and will be used in the rest of the analysis in this work.

In the case of tension (Fig. 4.2a), for the honeycomb arrangement ($RAI = 0$) we notice that damage appears the latest with the sharpest increase in damage at around an applied load of 42 MPa which coincides with the normal interfacial strength in 1. As expected, damage generally appears earlier and develops more gradually for higher numbers of RAI. Onset of plasticity is non-existent for any of the microstructures studied in tension. Note the tensile stress required to cause yielding in the homogenized material would be $\sigma_{\mathrm{yt}} = 121$ MPa, which is around 3 times greater than the applied stress of 40.5 MPa. Therefore, damage is fully dominated by normal interfacial damage, as will be studied in more detail in following sections.

We have also studied the sensitivity to different equivalent random arrangements: three different random distribution models with $RAI = 0.5$ were developed. Meaning that different equivalent microstructures can produce an equivalent randomness number in Eq. (3.1). Although not shown for the sake of clarity, we found that for $RAI = 0.5$, a $\approx 10\%$ variability in the fractional accumulated damaged occurs between different equivalent randomly distributed microstructures.

In compression (Fig. 4.2b) as expected, we find a similar trend to tension in terms of the evolution of damage initiation as the load is increased. The load at which 2% of interfacial segments become damaged for $RAI = 0.9$ is 109 MPa. Note that, due to damage localization, this load is slightly lower than the expected stress for damage initiation in favourly oriented segments at $\theta = 45°$ with a nominal stress of $2 * \tau = 126$MPa in the homogenized material, using the damage interface properties in Table 1. Contrary to tension loading, plasticity exists in the matrix during loading in compression for the studied cases. As depicted from Fig. 4.1c, localized plasticity develops at an applied load (at 109MPa) significantly lower than the general yield for compression of the matrix, $\sigma_{yc} = 176$ MPa. The Von Mises equivalent plastic strain, ϵ_{pl}, reaches localized

values of $\approx 0.3\%$, which is significant when compared to the elastic strains and therefore influencing in redistribution of the local stresses. The early damage development, particularly in microstructures with low RAI, indicate that damage is largely driven by the interfacial maximum shear stress. Nevertheless, the local stresses will be redistributed as localized plasticity occurs.
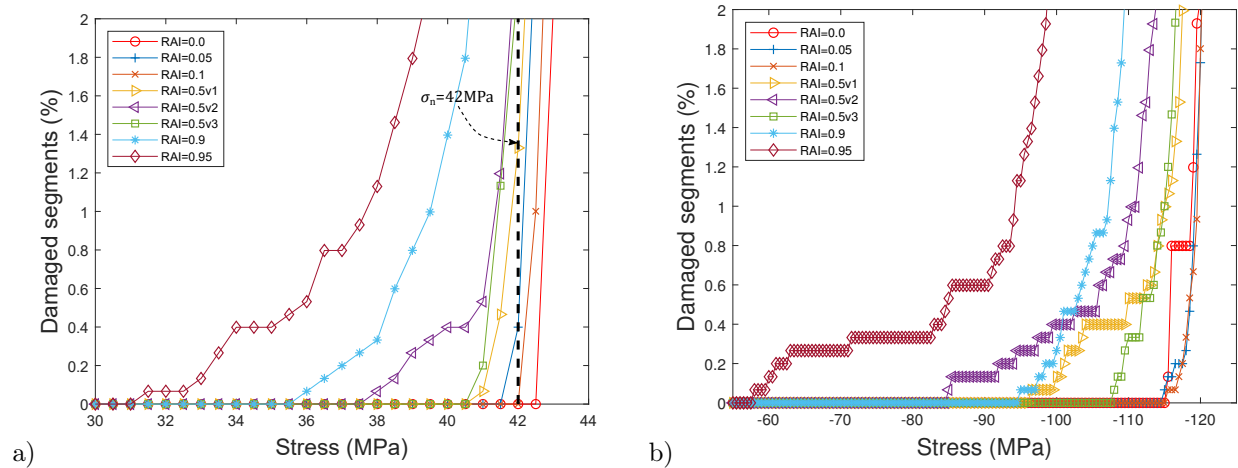

Figure 4.2: Evolution of the interfacial damage as a function of the applied load under tension (a) and compression (b). Each data point in the figure represents an increment of 0.5 MPA in loading.

4.4. Analysis of damage initiation angles

Here we study the damage fraction as a function of the angle θ, explained in Numerical Model section, formed between the normal of each segment composing the interface and the loading direction. Additionally, we show the variability of damage across fibers for each microstructure. For reference, we call interface segments to each edge connecting a pair of fiber-interface element (see Fig. 2.1). The angle range for the interface segments is $\theta \approx 15°$. For a given angle, there are as many interface segments as fibers. We show the fiber-to-fiber variability of the damage for a given angle. As discussed earlier, the chosen loads limits for the ratio of damaged segments to 2% are 40.5 MPa in tension and 109 MPa in compression.
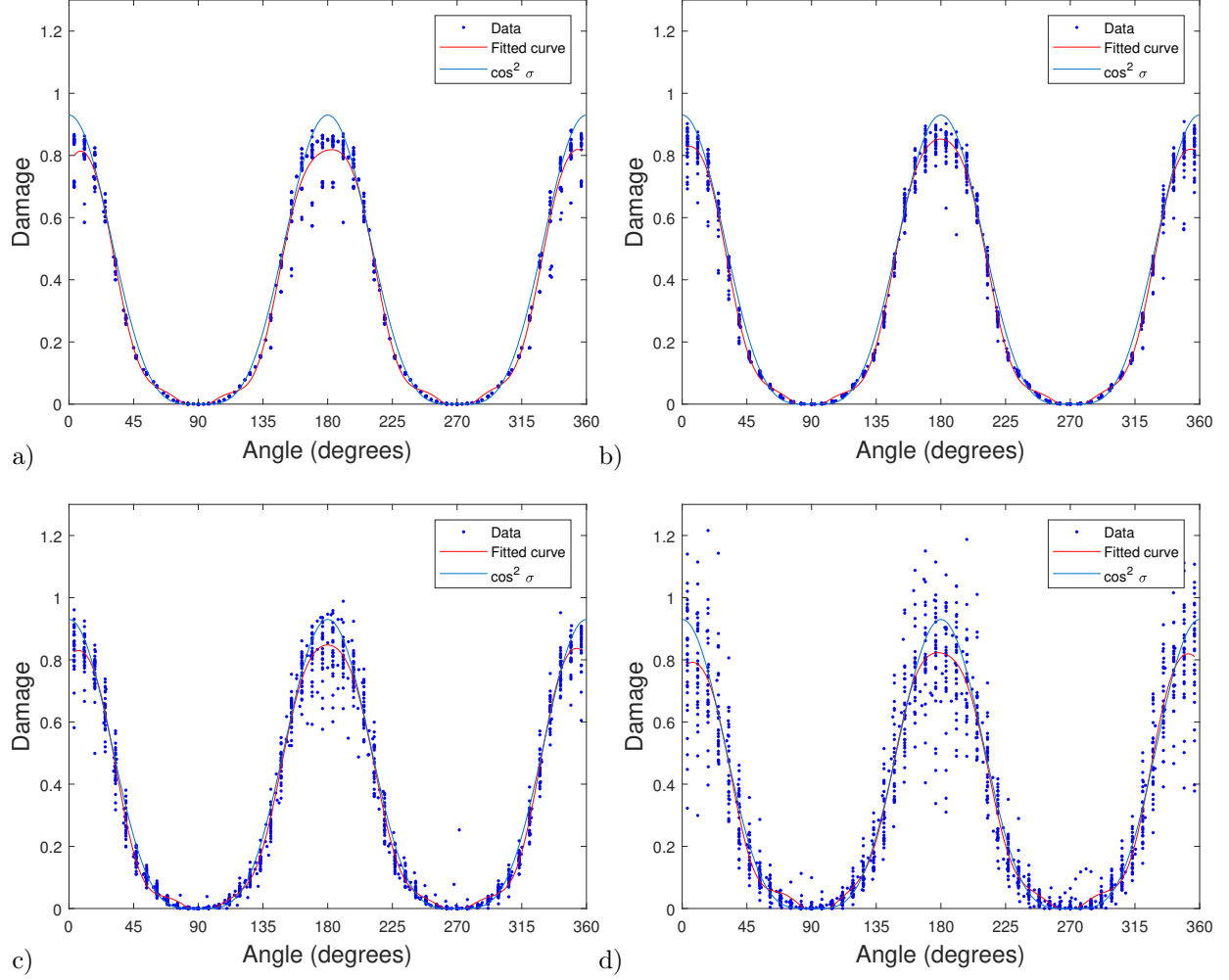
14

Figure 4.3: Total damage (according to Eq. 2.3) on each segment of the model for different random distributions (applied tension stress in the models is $\sigma = 40.5$ MPa). Fitted curves of the data are shown in the figures, as well as $\bar{\sigma} \cos^2$ function that reproduces the obtained results. a) $RAI = 0.0$ b) $RAI = 0.1$ c) $RAI = 0.5$ d) $RAI = 0.9$.

For uniaxial tension, the damage as a function of the angle is shown in Fig. 4.3, each point represents one fiber segment for the selected angle. We have obtained this value of damage by substituting the corresponding stress components in local coordinates at a segment into Eq. (2.3). For visualization purposes, two functions are superimposed in the figure. The first function is an arbitrary 7th degree polinomium that fits the data with coefficients of determination R^2: R^2=0.99 for $RAI = 0.0$, R^2=0.99 for $RAI = 0.1$, R^2=0.98 for $RAI = 0.5$ and R^2=0.91 for $RAI = 0.9$. The second function is $\bar{\sigma} \cos^2 \theta$, where $\bar{\sigma}$ refers to the value of the

uniaxial applied stress. The later function represents the normal stress to an interfacial segment around the fiber in the homogenized solid.

For each microstructure presented in Fig. 4.2, the detail of the damage in individual fibers is shown in Fig. 4.3. As the RAI increases, the variability of damage increases, leading to the highest number of damaged segments for $RAI = 0.95$. The results show that, as expected, the damage is highest at 0 and π angles for all microstructures. Moreover, at 0 and π angles the variability in damage is also highest i.e. more likelihood of fibre segments failing for these directions. The almost perfect match between the two functions reveals that the damage initiation is entirely dominated by the normal stress, rather than the shear stress, for all microstructures.

For uniaxial compression, the same procedure has been followed to plot Fig. 4.4. The arbitrary 7th order data fit function in this case has a correlation with coefficients of determination R^2: R^2=0.99 for $RAI = 0.0$, R^2=0.99 for $RAI = 0.1$, R^2=0.93 for $RAI = 0.5$ and R^2=0.76 for $RAI = 0.9$. The second function has been chosen as $\bar{\sigma}|\cos\theta\sin\theta|$, where $\bar{\sigma}$ refers to the applied stress in compression. The later function represents the shear stress to a interfacial segment in the homogenized solid. As in the case of tension, higher values of microstructure randomness results in higher number of damaged segments, also with the highest number of damaged segments for $RAI = 0.95$.
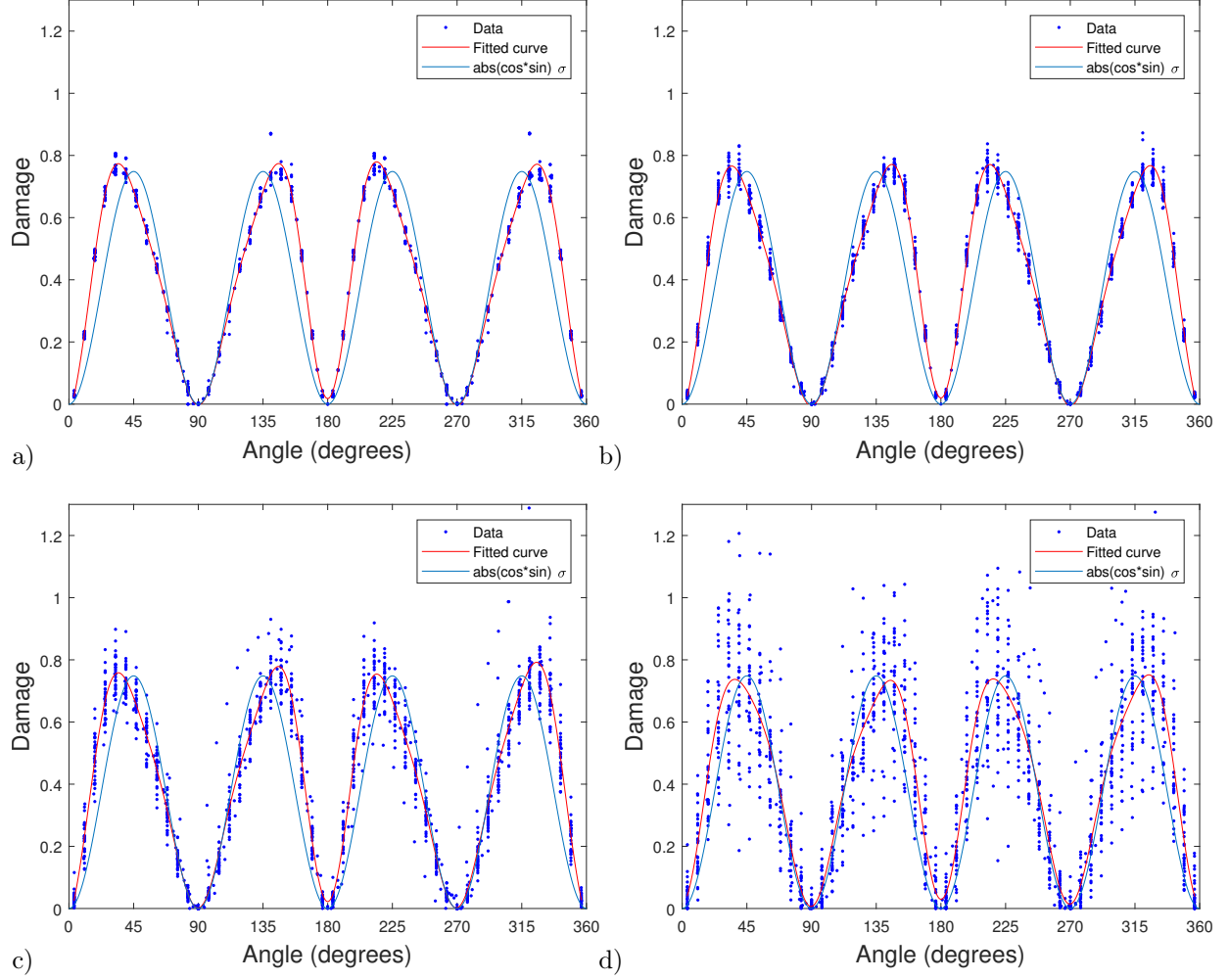
Figure 4.4: Total damage (according to Eq. 2.3) on each segment of the model for different random distributions (applied compression stress in the models is $\sigma = 109$ MPa). Fitted curves of the data are shown in the figures, as well as $\bar{\sigma}|\cos\theta\sin\theta|$ function that reproduces the obtained results. a) $RAI = 0.0$ b) $RAI = 0.1$ c) $RAI = 0.5$ d) $RAI = 0.9$.

There is a noticeable phase delay between the fitted polynomium and the $\bar{\sigma}|\cos\theta\sin\theta|$ function. The latter function, as expected, shows maximum damage by shear stress at $\theta = (1/2 + k)\pi/2$ (with $k = 0, 1, 2, 3$: $\theta = 45°, 135°, 225°$ and $315°$). From Fig. 4.4, it can be seen that maximum damage occurs between the maximum damage by shear stress and $\theta = k\,\pi/3 + \pi/6$ (with $k = 0, 2, 3, 5$: $\theta = 30°, 150°, 210°$ and $330°$), which are the least packed directions in the honeycomb arrangement ($RAI = 0$). It is observed that $\theta = k\,\pi/3 + \pi/6$ (with $k = 1, 4$: $\theta = 90°$ and $270°$) are also least packed directions, however, the resolved

shear stress in the homogenized solid are equal to zero for these directions, since they are perpendicular to the loading direction. Note that this assymmetry cannot be attributed to the elastic material anisotropy, since the material is only anisotropic in directions containing the component of the outplane coordinate axes i.e. X_1. As the RAI number increases, the fiber-to-fiber damage variability increases and thus the strength of the assymmetry between the two functions (maximum shear and least packed directions) weakens slightly. Damage development in individual fibers will be studied in the next section.

4.5. Shear and normal components of damage around individual fibers

In this section, the aim is to study the normal and shear contributions to interfacial damage. We arbitrarily choose individual fibers that represent the typical damage observed across the fibers, although damage around the other fibers is not shown for clarity purposes. For uniaxial tension in a microstructure with $RAI = 0$, Fig. 4.5a shows the damage to be highest at $\theta = 0°$ and $\theta = 180°$. This is consistent with the results shown in 4.3, confirming that the damage is almost completely dominated by the interfacial normal contribution. For all fibers in the $RAI = 0$ microstructure there is weak contribution to shear with maximums at $\theta = k\,\pi/4$ (with $k = 1, 3, 5, 7$: $\theta = 45°, \theta = 135°, \theta = 225°$, and $315°$). This is expected macroscopically for uniaxial loading along normal direction to the segment ($\mathbf{n}$), where the shear stress, $n_{\mathrm{s}} = \mathbf{s} \cdot \sigma \cdot \mathbf{n}$, is maximum at these angles for a stress state, σ, with $\mathbf{s} \cdot \mathbf{n} = 0$. For a typical fiber with $RAI = 0.9$ microstructure (Fig. 4.5b), damage asymmetry with respect to each $\pi/4$ quadrant appears in both shear and normal contributions. This is attributed to the local fields imposed by neighbouring fibers as plasticity is non-existent throughout the microstructure. Nevertheless, the normal interfacial damage still fully dominates the damage contribution rather than the shear damage contribution.
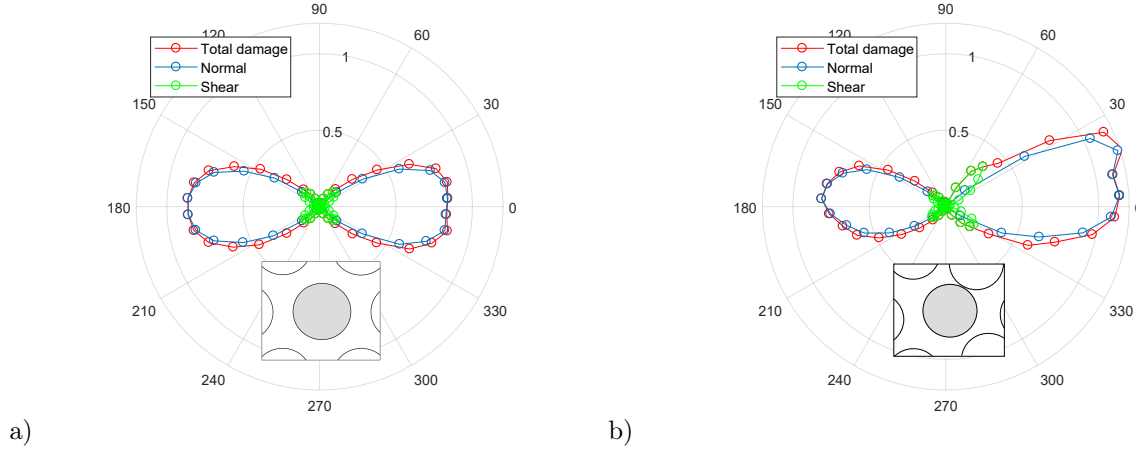
Figure 4.5: Shear and normal components of damage in polar coordinates in tension ($\sigma = 40.5$ MPa). Results shown for typical fibers in a) hexagonal distribution ($RAI = 0.0$) and b) $RAI = 0.90$

Next, we study the results of individual fibres in microstructures subjected to uniaxial compression. The results show that the shear damage to be highest nearby the region of $\theta = 5\,\pi/4$ (with $i = 1, 3, 5, 7$: $\theta = 45°, \theta = 135°, \theta = 225°$, and $315°$) for $RAI = 0$ (Fig. 4.6a) and for $RAI = 0.90$ (Fig. 4.6b).

In the previous section, it was noticed that the maximum damage is shifted from the directions with maximum shear towards the directions of least fiber packing with non-zero shear stress. In Fig. 4.6a, the peak is reached between $30°$ and $45°$. This may be attributed to the constraint imposed by the nearest fiber at $60°$ which prevents the connective matrix to relax the shear stress. At $45°$, although to a lesser extent, this constraint is still present, preventing the peak in shear stress to develop at this angle. At $30°$, the matrix channels between fibers can redistribute the stress in the fibers, analogously to the less carrying load observed along the matrix channels in Fig. 4.1d. In other words, the directional stiffness differences between $60°$, $45°$ and $30°$ directions, due to the fiber packing, results in a shifting of the $45°$ maximum shear stress expected in a geometrically isotropic material towards the lower stiffness direction at $30°$. In Fig. 4.4, it was shown that, as the R^2 increases this fiber-arrangement material anisotropy becomes weaker due to the stress redistribution imposed by local neighbouring fibres. An example of the stress redistribution around a fiber in a highly random fiber-arrangement microstructure is shown in Fig. 4.6b. Although the stress profile

in the neighbourhood of this fiber becomes complex, it appears that the maximum macroscopic shear stress (at 45°) is shifted towards the directions of least local packing directions.

The combined effect of thermal strains, subsequent loading and local neighbourhood can lead to variability of shear damage at the interface as depicted from Fig. 4.6. These results are consistent with previous results showing that the interfacial normal and tangential strengths have a strong influence on the macroscopic shear response [13]. Although the local compressive stress can be strongly influenced by the distance between local neighbouring fibers as well as localized plasticity (see Fig. 4.1), the results in Fig. 4.6 show that tension does not develop regardless of θ. This implies that damage by tension is non-existent, even for fibers embedded in highly random microstructures. Thus, contrary to the case for uniaxial tension, the total damage under macroscopic compression is almost completely dominated by the interfacial tangential contribution for all fibres in all microstructures.
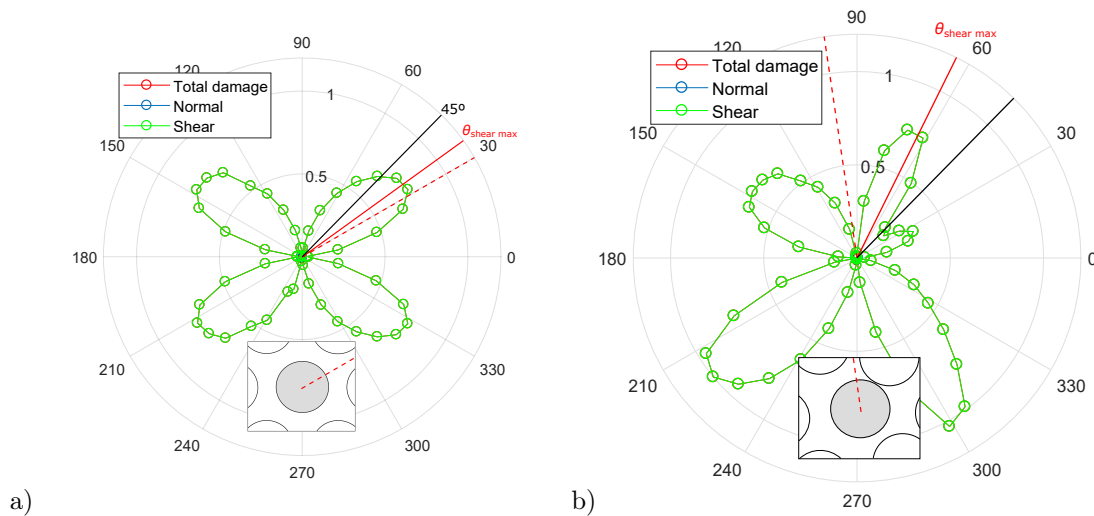

Figure 4.6: Shear and normal components of damage in polar coordinates in compression ($\sigma = 109$ MPa). Results shown for typical fibers in a) $RAI = 0$ and b) $RAI = 0.90$. Note the shear and total damage contributions are coincident because the normal damage is non-existent. 45° black lines represent maximum shear direction in the homogenized solid. Red continuous line show the angle where the total damage reaches a maximum and red dotted line shows the direction with most nearby interfacial distancing.

5. Conclusions

In this work, the interfacial damage initiation in a composite material reinforced by long fibers has been analysed through a finite element model. The cooling effect from manufacturing temperatures and a systematic random distribution of the fibers has been included in the study. Tension and compression conditions have been analysed for different random distributions.

Although only damage initiation has been considered, the microscale model is able to predict residual stresses induced during the manufacture and its influence on damage at fiber-matrix interfaces. Residual stresses are caused by heterogeneity in thermal properties and clearly affect the mechanical behaviour of the whole model, including the damage.

Microstructures have been generated according to the level of randomness with respect to the hexagonal arrangement (honeycomb pattern). The level of randomness is characterised by the minimum allowed distance between any two fibers. Using this method, the randomness of the model can be controlled and results are more consistent.

Due to the mismatch in thermal expansion between the fibers and the matrix, a thermal stress (residual stress) is expected after cooling from manufacturing temperature. The residual stress from the cooling superimposes on the loading stress prior to the loading.

Under tension conditions, the damage appears in the early stages of loading due to local damaged interfaces at nearer fibers. The normal interfacial strength dominates the damage initiation of the microstructure and nearness of surrounding fibers increase the interfacial stresses.

In compression, similar damage has been calculated for the early stages of the analysis. The damage is dominated by the shear component. Local distribution of fibers redistributes the maximum shear stresses, with influence of the least packed direction.

6. Acknowledgments

89197-C2-2-R. <mark>Doctorado industrial???</mark>

References

[1] Brewer JC, Lagace PA. Quadratic stress criterion for initiation of delamination. Journal of composite materials 1988;22(12):1141–55.

[2] Budiansky B, Fleck NA. Compressive failure of fibre composites. Journal of the Mechanics and Physics of Solids 1993;41(1):183–211.

[3] Canal LP, González C, Segurado J, LLorca J. Intraply fracture of fiber-reinforced composites: Microscopic mechanisms and modeling. Composites science and technology 2012;72(11):1223–32.

[4] Danzi F, Fanteria D, Panettieri E, Palermo M. A numerical micro-mechanical study of the influence of fiber–matrix interphase failure on carbon/epoxy material properties. Composite Structures 2017;159:625–35.

[5] Drucker D, Prager W. Soil mechanics and plastic analysis or limit design. Quart Appl Math 1952;10(2):157–65.

[6] Dugdale DS. Yielding of steel sheets containing slits. Journal of the Mechanics and Physics of Solids 1960;8(2):100–4. doi:10.1016/0022-5096(60)90013-2.

[7] Fleck NA, Budiansky B. Compressive failure of fibre composites due to microbuckling. In: Dvorak GJ, editor. Inelastic Deformation of Composite Materials. Springer New York. p. 235–73.

[8] Garcea SC, Wang Y, Withers PJ. X-ray computed tomography of polymer composites. Composites Science and Technology 2018;156:305–19. doi:10.1016/j.compscitech.2017.10.023.

[9] Giner E, Vercher A, Marco M, Arango C. Estimation of the reinforcement factor ξ for calculating the transverse stiffness e2 with the halpin–tsai equations using the finite element method. Composite Structures 2015;124:402–8.

22

[10] González C, LLorca J. Mechanical behavior of unidirectional fiber-reinforced polymers under transverse compression: Microscopic mechanisms and modeling. Composites Science and Technology 2007;67(13):2795–806. doi:10.1016/j.compscitech.2007.02.001.

[11] González D, Simonovski I, Withers PJ, Quinta da Fonseca J. Modelling the effect of elastic and plastic anisotropies on stresses at grain boundaries. International Journal of Plasticity 2014;61:49–63. doi:10.1016/j.ijplas.2014.03.012.

[12] Hashin Z. Failure criteria for unidirectional fiber composites. Journal of Applied Mechanics 1980;47(2):329–34. doi:10.1115/1.3153664.

[13] Hinz S, Omoori T, Hojo M, Schulte K. Damage characterisation of fibre metal laminates under interlaminar shear load. Composites Part A: Applied Science and Manufacturing 2009;40(6):925–31. doi:10.1016/j.compositesa.2009.04.020.

[14] Hojo M, Mizuno M, Hobbiebrunken T, Adachi T, Tanaka M, Ha SK. Effect of fiber array irregularities on microscopic interfacial normal stress states of transversely loaded UD-CFRP from viewpoint of failure initiation. Composites Science and Technology 2009;69(11):1726–34. doi:10.1016/j.compscitech.2008.08.032.

[15] Hull D, Clyne TW. An Introduction to Composite Materials. Cambridge University Press, 1996. Google-Books-ID: BRcdDu4bUhMC.

[16] Kim JK, Mai YW. Engineered Interfaces in Fiber Reinforced Composites. Elsevier, 1998. Google-Books-ID: qrjC9Yt8y6kC.

[17] LLorca J, González C, Molina-Aldareguía JM, Lópes CS. Multiscale modeling of composites: Toward virtual testing ... and beyond. Journal of the Minerals, Metals and Materials Society 2013;65(2):215–25. doi:10.1007/s11837-012-0509-8.

[18] Mallick PK. Fiber-Reinforced Composites: Materials, Manufacturing, and Design, Second Edition. CRC Press, 1993. Google-Books-ID: z0MIzzOFMqkC.

23

[19] Naya F, González C, Lopes C, Van der Veen S. Combined multi-scale simulations in fiber-reinforced composites. Conference: ECCM-16th European Conference on Composite Materials 2014;.

[20] Needleman A. An analysis of tensile decohesion along an interface ;38(3):289–324. doi:10.1016/0022-5096(90)90001-K.

[21] Rodríguez M, Molina-Aldareguía JM, González C, LLorca J. Determination of the mechanical properties of amorphous materials through instrumented nanoindentation. Acta Materialia 2012;60(9):3953–64. doi:10.1016/j.actamat.2012.03.027.

[22] Rodríguez M, Molina-Aldareguía JM, González C, LLorca J. A methodology to measure the interface shear strength by means of the fiber push-in test. Composites Science and Technology 2012;72(15):1924–32. doi:10.1016/j.compscitech.2012.08.011.

[23] Safarabadi M, Shokrieh MM. 8 - understanding residual stresses in polymer matrix composites. In: Shokrieh MM, editor. Residual Stresses in Composite Materials. Woodhead Publishing; 2014. p. 197–232. doi:10.1533/9780857098597.2.197.

[24] Segurado J, González C, Llorca J. A numerical investigation of the effect of particle clustering on the mechanical properties of composites. Acta materialia 2003;51(8):2355–69.

[25] Segurado J, LLorca J. Computational micromechanics of composites: the effect of particle spatial distribution. Mechanics of materials 2006;38(8-10):873–83.

[26] Sket F, Seltzer R, Molina-Aldareguía JM, González C, LLorca J. Determination of damage micromechanisms and fracture resistance of glass fiber/epoxy cross-ply laminate by means of x-ray computed microtomography. Composites Science and Technology 2012;72(2):350–9. doi:10.1016/j.compscitech.2011.11.025.

[27] Talreja R, Varna J. Modeling damage, fatigue and failure of composite materials. Elsevier, 2015.

[28] Totry E, González C, LLorca J. Failure locus of fiber-reinforced composites under transverse compression and out-of-plane shear. Composites Science and Technology 2008;68(3):829–39. doi:10.1016/j.compscitech.2007.08.023.

[29] Vajari DA. A micromechanical study of porous composites under longitudinal shear and transverse normal loading. Composite Structures 2015;125:266–76.

[30] Vaughan TJ, McCarthy CT. A combined experimental-numerical approach for generating statistically equivalent fibre distributions for high strength laminated composite materials. Composites Science and Technology 2010;70(2):291–7. doi:10.1016/j.compscitech.2009.10.020.

[31] Vaughan TJ, McCarthy CT. A micromechanical study on the effect of intra-ply properties on transverse shear fracture in fibre reinforced composites. Composites Part A: Applied Science and Manufacturing 2011;42(9):1217–28. doi:10.1016/j.compositesa.2011.05.004.

[32] Vogler TJ, Hsu SY, Kyriakides S. Composite failure under combined compression and shear. International Journal of Solids and Structures 2000;37(12):1765–91. doi:10.1016/S0020-7683(98)00323-0.